IEEE Access
Multidisciplinary | Rapid Review | Open Access Journal

Received April 11, 2017, accepted May 24, 2017, date of publication June 8, 2017, date of current version June 27, 2017.

*Digital Object Identifier 10.1109/ACCESS.2017.2712767*

# A Novel Technique for Robust and Fast Segmentation of Corneal Layer Interfaces Based on Spectral-Domain Optical Coherence Tomography Imaging

**TIANQIAO ZHANG[1,2], AHMED ELAZAB[3], XIAOGANG WANG[4], FUCANG JIA[1], JIANHUANG WU[1], GUANGLIN LI[1,5], (Senior Member, IEEE), AND QINGMAO HU[1,5]**

[1]Shenzhen Institutes of Advanced Technology, Chinese Academy of Sciences, Shenzhen 518055, China
[2]Shenzhen College of Advanced Technology, University of Chinese Academy of Sciences, Shenzhen 518055, China
[3]Computer Science Department, Misr Higher Institute for Commerce and Computers, Mansoura 35516, Egypt
[4]Shanxi Eye Hospital, Taiyuan 030002, China
[5]Key Laboratory of Human-Machine Intelligence-Synergy Systems, Shenzhen 518055, China

Corresponding author: Qingmao Hu (qm.hu@siat.ac.cn)

The work was supported in part by the Key Joint Program of National Natural Science Foundation and Guangdong Province of China under Grant U1201257, in part by the National Natural Science Foundation of China under Grant 61671440 and Grant 61672510, in part by the Shenzhen Key Technical Development under Grant CXZZ20140610151856719, and in part by the Shenzhen Key Basic Research under Grant JCYJ20160331191401141.

**ABSTRACT** A novel approach to segment corneal layer interfaces using optical coherence tomography images is presented. In this paper, we performed customized edge detection for initial location of interfaces, fitting the initial interfaces to circles via customized Hough transform, and refining interfaces by employing Kalman filtering to model the horizontal projectile motion of interface boundaries. Validation based on 20 B-scan images from 60 volumes shows that three layer interfaces in each image can be segmented within 0.52 s with an average absolute layer interface error below 5.4 $\mu$m. Compared with an existing method, we are able to yield significantly better or similar accuracy at a higher speed with inferior software environment. From the validation experiments based on images from normal human subjects, images with keratoconus and images with laser *in situ* keratomileusis flap, we showed that the proposed customized Hough transform for circles can represent the corneal layer interfaces more accurately. On the other hand, Kalman filtering can handle the heavy noise exhibited in the image, and can be adapted to shape variation in order to be closer to the real-layer interfaces. In conclusion, our approach can be a potential tool to quantify corneal layer interfaces in a clinical environment with lower computational expenses while maintaining high effectiveness.

**INDEX TERMS** Optical coherence tomography, Kalman filtering, Hough transform, corneal layer interface, image segmentation, fast algorithm.

## I. INTRODUCTION

Optical coherence tomography (OCT) has become an important optical signal acquisition and processing modality for imaging subsurface tissue structures with micrometer depth resolution in clinical ophthalmology [1]–[4]. The procedure is performed in a non-invasive and non-contact way, especially pertaining to the retina [1], [2], [5]–[11] and cornea [3], [4], [12]–[14]. Quantities derived from the segmented corneal layer interfaces/boundaries can provide information about the thickness and curvature, which are essential in diagnostic and surgical management of corneal edema, ocular hypertension, and endothelial function or refractive surgery [15]–[26]. Accurate segmentation is crucial as a few micrometers of corneal segmentation errors can lead to significant changes in the derived clinical parameters [22].

Several methods to segment corneal layer interfaces have been addressed with varying degrees of success. Li *et al.* [12], [13], [22] presented an algorithm for automatic corneal segmentation via exploring a combined parametric active contours and parabolic fitting algorithm. Eichel *et al.* [27] presented a semi-automated corneal segmentation method by using enhanced intelligent scissors and

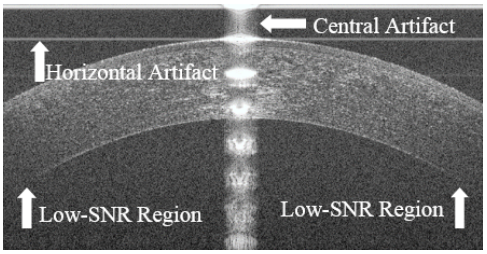


**FIGURE 1.** OCT corneal image with varying SNRs and artifacts, including low-SNR regions, horizontal artifacts, and central artifacts. This image is adapted from Image 3 of [30].

an energy minimizing spline. A threshold-based model was utilized by Shen *et al.* [28] to delineate the corneal anterior interface, without considering the posterior surface. Shu and Sun [29] developed a random sample consensus for circular fitting and a ąŕdivide-and-conqueręś strategy to extract inner and outer contours of the anterior chamber from time-domain OCT (TD-OCT) images. Unfortunately, none of the above algorithms can effectively handle images with low signal-to-noise ratio (SNR) regions or varying sources of artifacts such as central saturation and horizontal artifacts (Fig. 1).

Recently, more robust methods such as graph theory and level set were explored to achieve better segmentation. LaRocca *et al.* [30] employed graph theory to segment central corneal layer interfaces for better robustness to artifacts. Williams *et al.* [31] proposed level set based shape prior model for automatic segmentation of corneal anterior and posterior interfaces. Later, they extended the graph theory approach and genetic algorithms to reconstruct three dimensional (3D) surface maps of cornea [32]. However, methods using graph theory or level set result in high computational costs [5]–[7], [30]–[32].

In our previous work [33], we employed Kalman filtering [34], customized active contour and curve smoothing on retinal SD-OCT images to show promising performance in terms of speed and robustness to different sources of artifacts. Because the cornea and retina have different structures and different types of artifacts, the method cannot be directly applied to segment corneal OCT images. The main novelties of this study are summarized as follows.

Firstly, difference of mean intensity, inspired by the one-dimensional (1D) Haar wavelet [35] and the difference of Gaussian [36], is employed for edge detection, followed by smoothing based on Savitzky-Golay algorithms [37] for initial localization of corneal layer interfaces. Secondly, a customized Hough transform (HT) for circles (HTC) based on the theorem of perpendicular bisection of a chord is introduced to reduce the computational cost to fit layer interfaces to circles. Thirdly, we model corneal layer interfaces as parabolic curves with parameters estimated from the derived circles. Finally, based on modeling each corneal layer interface as a horizontal projectile motion of particles, Kalman filtering [34] is employed to track boundaries (particles) in each interface of a single image to yield fast and accurate layer interfaces.

The rest of the paper is organized as follows. Section II is devoted to method. Experimental results are then described in Section III while discussion and conclusion are given in Section IV.

## II. PROPOSED METHOD

An OCT imaging system can generate B-scans (i.e., two dimensional (2D) images) by gathering a number of A-scans (axial or depth direction) from adjacent transverse (lateral direction) positions [1]. In this paper, we use the following denotations: $H$ for the depth of an A-scan, $W$ for the width of a B-scan, $y$ for the depth coordinate (ranging from 0 to ($H$-1)), $x$ for the lateral coordinate (ranging from 0 to ($W$-1)), and f($x$,$y$) for the grayscale/intensity at pixel ($x$,$y$).

We will divide Section II into five subsections, which respectively deals with preprocessing, detecting layer interfaces using customized edge detection, customized HTC, approximating axial coordinates for apexes of Bowman and endothelium, and refining layer interfaces through Kalman filtering. Figure 2 shows the flowchart of the method to be elaborated in more details.

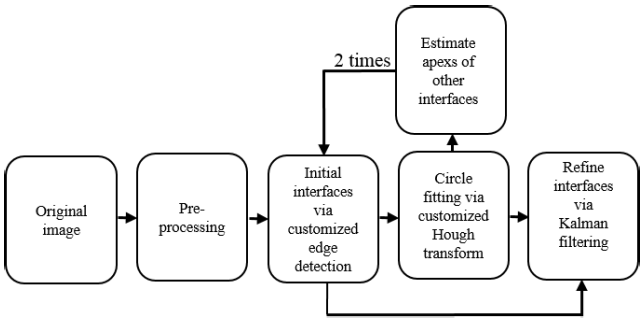


**FIGURE 2.** Flowchart of our proposed method to segment corneal layer interfaces from B-scan images.

### A. PREPROCESSING

We divide the pre-processing stage into four steps: image resizing, approximating the lateral coordinate of corneal apex, approximating the axial coordinate of epithelial apex, and suppression of horizontal artifact.

#### 1) IMAGE RESIZING

The image is resized to isotropic pixel sizes in order to facilitate modelling central corneal layer interfaces with circles. The width, height and the grayscales of both the original and resized images are denoted as $W$, $H$, and $f(x, y)$ respectively.

#### 2) APPROXIMATING LATERAL COORDINATE OF CORNEAL APEX

Firstly, each column of the image is projected along the axial direction [30] based on the following equation:

$$g(x) = \frac{1}{H}\sum_{y=0}^{H-1} f(x, y) \tag{1}$$

The grayscale of the maximum of $g(x)$ and its $x$ position are denoted as $g_{max}$ and $p_{max}$, respectively.

Then, the image is divided into three regions with equal width denoted as regions *I*, *II*, and *III*, from left to right, in which only the central region *II* is assumed to hold the central artifact [30].

Next, the average grayscale for region *I* and region *III* are denoted as $m_I$ and $m_{III}$ respectively. Then, we set the threshold to detect the central artifact as $T_{cent}$, which is defined:

$$T_{cent} = \rho \times S_{I,III} + (1.0 - \rho) \times g_{max}, 0 < \rho < 1.0$$
$$S_{I,III} = (m_I + m_{III})/2 \quad (2)$$

Here, $\rho$ is a predefined constant that is set as 0.5.

Finally, we search from the position $p_{max}$ to the leftmost and the rightmost in region *II* to find the lateral coordinates with $g$(x) being greater than $T_{cent}$, and denote them as $p_{left}$ and $p_{right}$, respectively. The $x$ coordinate of the corneal apex can be approximated as:

$$A_x = (p_{left} + p_{right})/2 \quad (3)$$

Figure 3 shows the derived positions of central artifact.

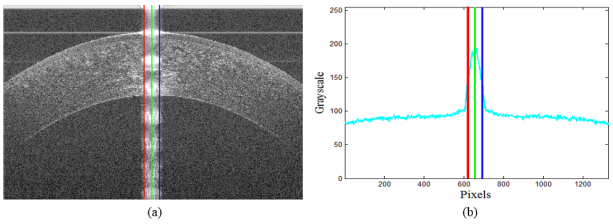


**FIGURE 3.** An OCT corneal image (from Fig. 1) and its vertical projection: (a) an original OCT corneal image with colored lines for the leftmost (in red), central (in green) and rightmost (in blue) position of the central artifact and, (b) the average grayscale curve (in cyan) of each column of (a).

#### 3) APPROXIMATING AXIAL COORDINATE OF EPITHELIAL APEX

To begin with, each row of the image is projected along the lateral direction using:

$$g(y) = \frac{1}{W} \sum_{x=0}^{W-1} f(x, y) \quad (4)$$

The epithelial apex corresponds to the local maxima, however, not necessarily the maximum due to horizontal artifacts (Fig. 4). To obtain a robust and precise y position of the epithelial apex, forward difference is performed for $g(y)$ as follows:

$$g'(y) = g(y + 1) - g(y) \quad (5)$$

The maximum of $g'(y)$ corresponds to the $y$ coordinate of the epithelial apex (Fig. 4).

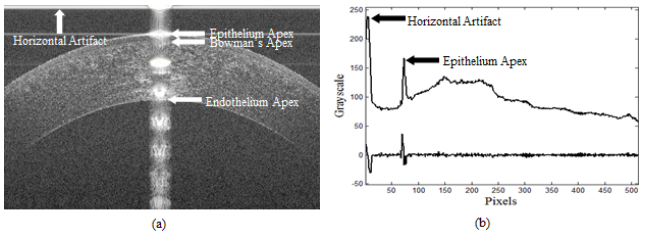


**FIGURE 4.** An OCT corneal B-scan (from Fig. 1) and its lateral projection: (a) an original OCT corneal image with vertical arrow pointing to the horizontal artifact, and horizontal arrows pointing respectively to the epithelial apex, Bowman's apex, and endothelium apex, and (b) the average grayscale curve of all rows of (a) (top) and its forward difference curve (bottom).

#### 4) SUPPRESSION OF HORIZONTAL ARTIFACT

To make the delineation of corneal layer interfaces more reliable, we suppress the horizontal artifact based on subtracting the mean signal for each row (Fig. 5). For simplicity of denotation, the image after artifact suppression is still denoted as $f(x,y)$.

### B. DETECTING LAYER INTERFACES THROUGH CUSTOMIZED EDGE DETECTION

There are two characteristics of corneal layer interfaces: layered structures, and the dark-to-bright or bright-to-dark intensity transitions in axial direction. These distinct properties are to be explored in three steps: derivation of region of interest (ROI) of layer interfaces, flattening the ROI so that edges are almost horizontal, and customized edge detection.

#### 1) DERIVATION OF THE REGION OF INTEREST OF LAYER INTERFACES

An ROI of each layer interface is expressed as a circular ring. From Section II-A, the approximated lateral and axial coordinates of the center (epithelial apex) are available. In addition, we can know its radius from prior knowledge (7.7mm) [39]. Thus, a circle $C_{init}^{epithe}$ being the central curve of ROI for air-epithelium interface can be determined. Similarly, ROIs for the other two layer interfaces can be constructed. They are given in Section II-D as they will need determination of the epithelium interface, while radii can be determined from prior knowledge (6.8 mm for endothelium-aqueous interface, 7.6 mm for epithelium-Bowman's interface) [39]. Half heights of the circular rings are predefined constants in this study, being 30 pixels for air-epithelium interface, 40 pixels for endothelium-aqueous interface, and 10 pixels for epithelium-Bowman's interface. The heights of the circular rings are carefully chosen to decrease the computational cost as well as to include the real interfaces due to the error in approximating the centers. Figure 5(a) shows the derived ROI of epithelium interfaces.

#### 2) IMAGE FLATTENING WITHIN THE REGION OF INTEREST

Once the ROI of each layer interface is determined, the ROI becomes flattened with respect to the derived layer interface.

Specifically, the flattening process is carried out this way: for each column $x$, the column will move ($C_{init}$ (y)-$A_y$+$H_1$) upwards with $H_1$ being the half height of the ROI in the axial direction, $C_{init}$ ($y$) being the $y$ coordinate of the pixel in the original image, and $A_y$ being the $y$ coordinate of the apex of each layer interface. In this way, the central curve becomes a horizontal line. Note that the layer interfaces are determined after obtaining the edge through Section II-B-3 using customized edge detection. They are curved to obtain the corresponding coordinates in the resized image.

### 3) CUSTOMIZED EDGE DETECTION

Once the ROI of each layer interface is flattened, the layer interface becomes almost horizontal to facilitate edge detection. Edges are detected through calculating the difference of intensity means column-wise using the following formula:

$$D_j(x) = \frac{1}{H_{ROI} - j} \sum_{y=j}^{H_{ROI}-1} f(x, y) - \frac{1}{j} \sum_{y=0}^{j-1} f(x, y) \qquad (6)$$

where $j$ is in the range from 1 to $H_{ROI}$-1, notably with $H_{ROI}$ being the height of the flattened ROI which is the height of the circular ring. In this paper, we search for the maximum absolute value of $D_j(x)$ for each $x$ as the edge pixel at column $x$. Note that Eq. (6) can be used with a low computational complexity by employing a 1D integral image [35].

After edges are detected using this equation, Savitzky-Golay filters [37], [46] are employed for curve smoothing of the layer interface with the order of the polynomial being 1 and a neighborhood size of 20 pixels. The edge detection through the equation followed by Savitzky-Golay filtering is called customized edge detection in this paper. Figure 5 shows the detected edges for air-epithelium interface through customized edge detection.

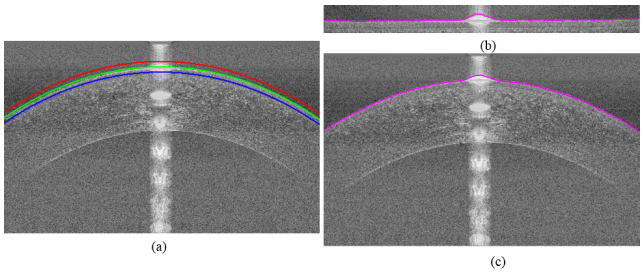


**FIGURE 5.** ROI determination and edge detection for air-epithelium of Fig. 1: (a) ROI of air-epithelium, where green curve, red curve and blue curve are central curve, top limit and bottom limit of the ROI respectively, (b) customized edge detection within the flattened ROI, and (c) approximated layer interface shown by the color magenta.

## C. HOUGH TRANSFORM FOR CIRCLES

The cornea of normal eyes is of a nearly spherical structure [38]. According to the Gullstrand eye model, the cross-section perpendicular to the optic axis and passing through the eye, intersects epithelium and endothelium of the cornea to contain two circles, with their radii being 7.7 mm and 6.8 mm respectively [39]. Since the OCT is a cross-sectional imaging, it is reasonable to approximate the central corneal layer interfaces with circles [38], [39]. However, in order to handle shape variability due to pathology such as keratoconus, parabolic curves are proposed to approximate spherical as well as near spherical corneal surfaces.

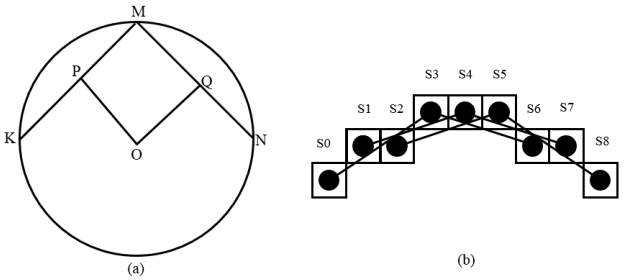


**FIGURE 6.** Hough transform for circles and its voting strategy: (a) line segments bisecting a chord of a circle will pass through the center of the circle, and (b) sequential equal-interval (in x direction) triples for voting the center.

A parabolic curve has four parameters, including the coordinates of the vertex ($x_v$,$y_v$), its curvature, and its orientation [40]. Here, we propose to estimate the parameters of a parabolic curve from its inscribed circle. It can be proven that a horizontal projectile motion whose trajectory falls into the family of parabolic curves can be constrained by its inscribed circle (see Section II-E). Then, an HTC is employed to accelerate the voting process.

HT is one of the most popular approaches for circle detection [41], [42]. A customized HTC based on bisection of a chord is presented to reduce the computational complexity.

For circle detection, the following two geometric properties are employed: a circle is uniquely determined by three non-collinear points, and the line segment that bisects a chord of a circle will pass through the center of the circle [43] (Fig.6).

Here, we introduce one triple on a circle (Fig. 6) and denote it as $KMN$ which consists of three points $K(x_K,y_K)$, $M(x_M,y_M)$, and $N(x_N,y_N)$. Since $OP$ and $OQ$ bisect the line segments $KM$ and $MN$ respectively, we have:

$$(y_O - y_P) \times (y_K - y_M) + (x_O - x_P) \times (x_K - x_M) = 0 \qquad (7)$$

$$(y_O - y_Q) \times (y_M - y_N) + (x_O - x_Q) \times (x_M - x_N) = 0 \qquad (8)$$

By Cramer's rule [44], the center $(x_0,y_0)$ can be computed as:

$$x_O = \frac{\begin{vmatrix} (x_K - x_M) & (y_Q \times y_M + x_Q \times x_M - y_Q \times y_N - x_Q \times x_N) \\ (y_K - y_M) & (y_P \times y_P + x_P \times x_K - y_P \times y_M - x_P \times x_M) \end{vmatrix}}{\begin{vmatrix} (x_K - x_M) & (y_K - y_M) \\ (x_M - x_N) & (y_M - y_N) \end{vmatrix}} \qquad (9)$$

$$y_O = \frac{\begin{vmatrix} (x_K - x_M) & (y_P \times y_P + x_P \times x_K - y_P \times y_M - x_P \times x_M) \\ (x_M - x_N) & (y_Q \times y_M + x_Q \times x_M - y_Q \times y_N - x_Q \times x_N) \end{vmatrix}}{\begin{vmatrix} (x_K - x_M) & (y_K - y_M) \\ (x_M - x_N) & (y_M - y_N) \end{vmatrix}} \qquad (10)$$

The existence condition for $(x_0,y_0)$ is:

$$(x_K - x_M) \times (y_M - y_N) - (x_M - x_N) \times (y_K - y_M) \neq 0 \tag{11}$$

which is equivalent to the non-collinearity of the three points $K$, $M$ and $N$.

Once the contour is derived from the customized edge detection, we can obtain the circle through the customized HTC. Let the distance of adjacent points of each triple in axial direction be $Dist_x$ pixels, the $x$ coordinate of pixel $K$ will be from 0 to $(W - 2 \times Dist_x - 1)$. The voting of HTC includes the center followed by the radius.

For computational efficiency, we sequentially select the consecutive triples with the difference in $x$ coordinate between two neighbor points of a triple being $Dist_x$. The proposed method requires only a 1D array whose length is $(W - 2 \times Dist_x - 1)$ for voting the center (Fig. 6). Although the intersection of two line segments that bisect two chords of a circle are 2D and therefore needs a 2D accumulator array, the 2D accumulator array can be confined in a small region (200 × 200 pixels, see below). After detecting the possible center, the 1D radius histogram of the distances between all edge points from the center can be utilized to compute the radius and verify the circle. By this technique, the overall computational load of the proposed HTC method is substantially decreased.

Specifically, for the dataset from [30], the searching parameters are set from experiments as below. The cell size in $x$ and $y$ directions for the Hough space of the center and the cell size for the radius histogram are all one pixel. Let the radius be $R_c$ pixels, then the searching ranges for the circle center in $x$ and $y$ directions and for radius are $[A_x - 100, A_x + 100]$, $[A_y + R_c - 100, A_y + R_c + 100]$ and $[R_c - 100, R_c + 100]$, respectively. Figure 7 shows the derived circle using the customized HTC for segmenting the air-epithelium boundary interface.

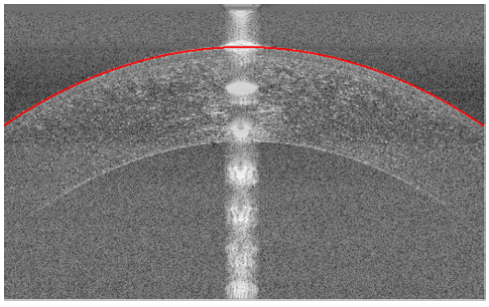

**FIGURE 7.** Derived circle using the customized HTC for segmenting the air-epithelium interface of Fig. 1.

### D. APPROXIMATING AXIAL COORDINATES FOR APEXES OF BOWMAN AND ENDOTHELIUM

Similar to the presentation in Section II-A-3, we approximate axial coordinates of apex of Bowman and endothelium, which are essential to detect epithelium-Bowman's interface and endothelium-aqueous interface, respectively. These coordinates are determined in four steps.

Firstly, to reduce impacts of central artifact, the grayscales of each pixel at center artifact regions are set to zero. Secondly, we flatten the image based on the segmented air-epithelium interface. Thirdly, each row of the flattened image is projected along the lateral direction using Eq. (4). Fourthly, to obtain a robust and precise y position of the apex of endothelium and Bowman, forward difference is performed for $g(y)$ according to Eq. (5).

The positions of the maximum of $g'(y)$ over the region 400–800 $\mu$m below the air-epithelium interface and the minimum of $g'(y)$ below the air-epithelium interface correspond to the $y$ coordinates of the Bowman's apex and the endothelium apex, respectively.

### E. KALMAN FILTERING TO MODEL HORIZONTAL PROJECTILE MOTION

In this subsection, we first show that the parabola, which is tangent to a circle at the vertex and intersects the circle, is uniquely determined.

As shown in Fig.8, suppose that the parabola $\beta$ is tangent to a circle $\alpha$ at the origin point $M(0,0)$, and intersects at point $N(x_N, y_N)$, the center of the circle is $O(x_O, y_O)$.

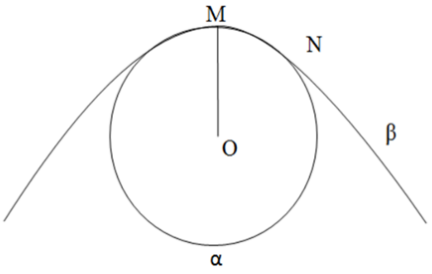


**FIGURE 8.** A parabola and its inscribed circle, where the parabola $\beta$ is tangent to a circle $\alpha$ at the origin point $M$, and intersects at point $N$, with the center of the circle being $O$.

Then, equations of the parabola and the circle can be written as:

$$y = \frac{1}{2}ax^2 \tag{12}$$

$$(y - r)^2 + x^2 = r^2 \tag{13}$$

where $a$ and $r$ are the coefficient of the parabola and the radius of the circle, respectively. As the circle and the parabola intersect at point $N$, we can determine $a$ by solving equations (12) and (13):

$$a = 2(r - \sqrt{r^2 - x_N^2})/x_N^2 \tag{14}$$

which relates the parabola and the circle. Here, $r$ is derived from HTC for each layer interface, and $x_N$ is set as the maximum $x$ coordinate of the fitted circle apart from its center.

As shown in Fig.9, each layer interface of the cornea may be analogous to a pair of trajectories of particle projectile

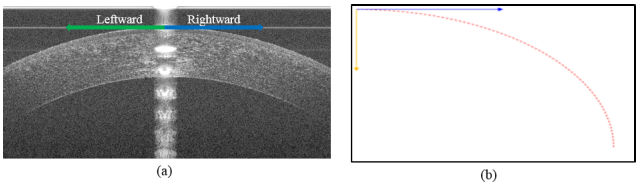


**FIGURE 9.** The pair of horizontal projectile motion for Fig.1: (a) an original OCT corneal image with colored arrows for opposite horizontal directions, and (b) the horizontal projectile motion curve with constant vertical downward acceleration and constant rightward velocity based on the right part of (a).

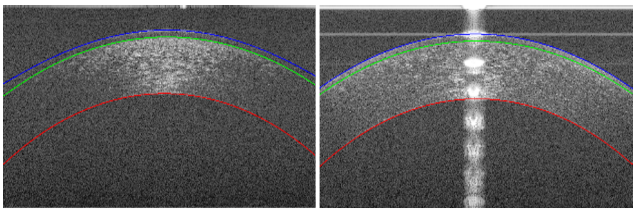


**FIGURE 10.** Refined interfaces using the Kalman filtering modeled with horizontal projectile motion, where blue, green and red curves are respectively for the air-epithelium, epithelium-Bowman's, and endothelium-aqueous layer interfaces based on (a) image 1; and (b) Fig.1.

motion from the apex of the layer interface in the two opposite horizontal directions. In light of the great success in control domain [45], Kalman filtering was introduced to track adjacent layer interfaces frame by frame [33]. By extending this approach, we explore horizontal projectile equation based on Kalman filtering to approximate the adjacent interface points for each corneal layer interface. The horizontal projectile motion whose trajectory is parabola is given by Eqs. (15) and (16). These are based on the condition of a constant acceleration [47]:

$$y(t) = y(t-1) + v_y(t-1) \times \Delta t + \frac{1}{2} \times a_y \times (\Delta t)^2 \quad (15)$$

$$v_y(t) = v_y(t-1) + a_y \times \Delta t \quad (16)$$

where $y$, $v_y$ and $a_y$ are the $Y$ coordinate, the speed and the acceleration of the adjacent layer boundaries being tracked, $t$, $t$-1 and $\Delta t$ (let $\Delta t$ = 1) being the current time, the previous time and the time interval respectively. Constant $a_y$ represents the vertical downward acceleration of the particle projectile motion, as determined by Eq. (14). In this paper, we denote the time in $x$ axis (i.e., $t$ is replaced with $x$), with $x$, $x$-1 and $\Delta x$ respectively pertaining to the current layer interface point, the previous interface point and the space interval in $x$ direction.

Furthmore, after replacing $t$ with $x$, Eqs. (15) and (16) can be written in a matrix form using Eq. (17):

$$\Phi(x) = A\Phi(x-1) + Ba_y \quad (17)$$

where $\Phi$, $A$ and $B$ are the 2D vector, the state transfer matrix and the control input matrix, being $\Phi = \begin{bmatrix} y \\ v_y \end{bmatrix}$, $A = \begin{bmatrix} 1 & \Delta x \\ 0 & 1 \end{bmatrix}$ and $B = \begin{bmatrix} 0.5 \\ 1 \end{bmatrix}$, respectively.

The covariance can be estimated as below:

$$\hat{P}(x) = AP(x-1)A^T \quad (18)$$

Here, $T$ represents matrix transposing, $\hat{}$ for the estimated value.

The correction equation is then given by:

$$K(x) = \hat{P}(x)H^T(H\hat{P}(x)H^T + R)^{-1} \quad (19)$$

where $H$ is [1 0], $R$ is the standard deviation of the measurement noise. $K$ will be adaptive to $R$, i.e., the components of $K$ will be smaller when $R$ is large, and larger otherwise. The state $\Phi$ can be updated using:

$$\hat{\Phi}(x) = A\hat{\Phi}(x-1) + K(x)(Z(x) - A\hat{\Phi}(x-1)) \quad (20)$$

where $Z(x)$ is the $y$ coordinate of current layer interface point derived from the customized edge detection (Section II-B-3). Finally, the covariance $P$ can be updated:

$$P(x) = (I - K(x)H)\hat{P}(x) \quad (21)$$

where $I$ is the identity matrix.

In summary, two phases (prediction by Eqs.(17) and (18), and updating by Eqs. (19)-(21)) of Kalman filtering are applied to obtain the state with minimum variance. Figure 10 shows the refined corneal layer interfaces based on the Kalman filtering model.

## III. EXPERIMENTS

Experiments were carried out to validate the proposed method on 20 images selected randomly from a pool of 60 SD-OCT corneal volumes from both eyes of 10 normal subjects, which was provided by [30]. The performance of the proposed method was then compared with that of [30] using the same dataset. Our algorithm has been implemented on a personal computer without parallel processing (Matlab program, 32-bit OS, Intel core i5-2320 CPU at 3.3 GHz and 4 GB RAM). The algorithm [30] implemented parallel processing with 8 threads (Matlab program, 64-bit OS, Intel (R) Core (TM) i7 CPU 860 at 2.80 GHz and 16 GB RAM).

For each corneal layer interface, we computed the average absolute position difference in layer interface between the automatic and manual delineation for quantification. We also calculated the average absolute position difference in layer interface between two gradersąŕ delineations [30] to show the variability by eye graders, which is a reflection of difficulties in identifying the layer interfaces.

The parameter $\rho$ determines the proportion of mean of $m_I$ and $m_{III}$ in the threshold $T_{cent}$ (Eq.(2)). We altered the $\rho$ in the range from 0.20 to 0.80 to yield similar segmentation accuracy (with the air-epithelium interface, epithelium-Bowman's interface and endothelium-aqueous interface showing a difference of 0.4±0.3 pixels, 0.7±0.4 pixels and 1.8±2.0 pixels respectively) and same time consumption. In this study, $\rho$ is fixed as the median value of the range to be 0.5.

**TABLE 1. Comparison of the existing method with the proposed measurement of corneal layer interfaces of 20 images of normal eyes.**

| | Comparison between two manual graders | | | Comparison between automatic and manual segmentations | |
|---|---|---|---|---|---|
| | first expert manual grader to self | second trained manual grader to self | between two manual graders | LaRocca's method | proposed |
| corneal layer interface | mean error±SD | mean error±SD | mean error±SD | mean error±SD | mean error±SD |
| first interface | $0.46 \pm 0.25$ | $1.16 \pm 0.76$ | $1.50 \pm 0.43$ | $0.55 \pm 0.43$ | $0.44 \pm 0.37$* |
| second interface | $0.76 \pm 0.42$ | $1.11 \pm 0.92$ | $1.24 \pm 0.52$ | $0.85 \pm 0.55$ | $0.72 \pm 0.58$* |
| third interface | $1.49 \pm 2.28$ | $2.46 \pm 3.03$ | $2.07 \pm 2.27$ | $1.66 \pm 2.15$ | $1.59 \pm 2.04$ |

Note: The first, second and third interfaces are respectively air-epithelium interface, epithelium-Bowman's interface, and endothelium-aqueous interface; First Expert (second trained) manual grade to self represents intra-observer repeatability of the first expert (second trained) manual grader; SD for standard deviation; * for significant difference ($p<0.05$); and the pixel size being 3.4 $\mu$m.

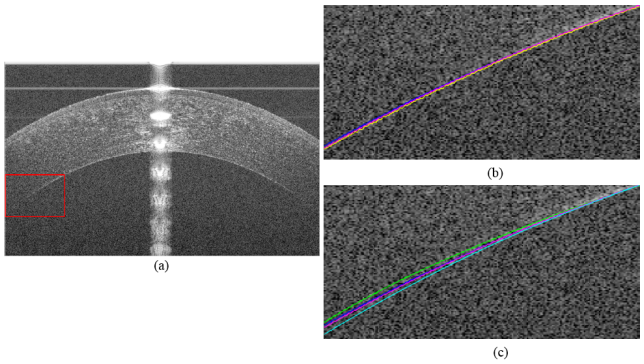


**FIGURE 11. Comparison with the segmentation of [30] for the endothelium-aqueous layer interface with the ground truth delineation in blue: (a) image of Fig. 1 with a red rectangle to specify the local image for comparison, (b) the delineated layer interfaces within the local image by the proposed method (magenta), and [30] (yellow), and (c) the delineated layer interfaces within the local image of the proposed method (magenta), $V_B$ (green) and $V_A$ (cyan).**

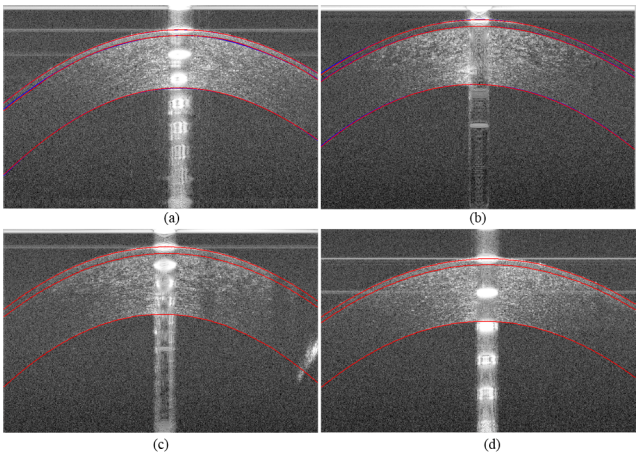


**FIGURE 12. Robustness test for the proposed method with various artifacts, where the delineations of layer interfaces of the ground truth are in blue while the segmented layer interfaces of the proposed method are in red. Note that: there are no ground truths for (c) and (d) as they are from the training set: (a) the image with relocated apex, and prominent central and horizontal artifacts (Image 2 of the 20 test images), (b) the image with low-SNR, a central artifact, and a hyporeflective region between the epithelium surface and the Bowman's layer (Image 7 of the 20 test images), (c) the image with an eyelash artifact and a prominent central artifact, and (d) the image with a horizontal artifact blow the apex of air-epithelium interface and a prominent central artifact.**

### A. COMPARISON WITH A STATE-OF-THE-ART METHOD

We compared our proposed method with that of LaRocca *et al.* [30] using their dataset and their manual segmentation as reference of normal eyes. The 60 volumes were acquired by Bioptigen Inc (Research Triangle Park, NC, USA) SD-OCT imaging system fitted with a corneal adapter. The commercial system measured B-scan pixel sampling resolution being $6.1\mu m \times 4.6\mu m$, and a lateral sampling measured peak sensitivity of 104 dB at 50 *ms* imaging time per B-scan. Only 20 B-scans that are randomly selected from the 60 volumes were manually delineated by two experts (one junior and one senior) and the manual delineation by the senior expert was taken as the reference. Figure 11(b) shows the comparative segmentation results based on one normal image.

It took an average of 521 ms to automatically derive the 3 layer interfaces of an image on a personal computer. Distribution of the segmentation time (521 *ms*) is as follows: pre-processing (93 *ms*), initial interfaces via customized edges detection ($22\ ms \times 3 = 66\ ms$), circle fitting via customized HTC ($73\ ms \times 3 = 219\ ms$), refining interfaces via Kalman filtering ($35\ ms \times 3 = 105\ ms$), and un-resizing (38 *ms*). Here, $\times$ 3 was used to process three interfaces for each image.

The comparison results between two experts as well as between the proposed method and [30] are summarized in Table 1.

### B. VALIDATION ON IMAGES WITH VARIOUS ARTIFACTS AND PATHOLOGICAL IMAGES

Images with relocated apex deviating from the center, hyporeflective region, eyelash artifact, and horizontal artifact below the apex are tested and shown in Fig.12 to highlight the robustness of the proposed algorithm. We also tested the proposed method on the pathological image datasets. The dataset obtained through RTVue-XR OCT (Optovue Inc., USA) was provided by Shanxi Eye Hospital, which includes 20 images with laser in-situ keratomileusis (LASIK) flap from 13 patients, and 10 images with abnormally steep curvatures (keratoconus) from 5 patients. As shown in Fig.13 and Table 2, our method can perform well on both images of corneal with keratoconus and with LASIK flap.

**TABLE 2. Comparison between automatic and manual segmentation for measurement of corneal layer interfaces of 20 images with LASIK flap and 10 images with keratoconus.**

| | Images with LASIK flap | | Images with keratoconus | |
|---|---|---|---|---|
| | between two manual graders | proposed vs the senior | between two manual graders | proposed vs the senior |
| Corneal layer interface | mean error±SD | mean error±SD | mean error±SD | mean error±SD |
| first interface | $0.42 \pm 0.27$ | $0.38 \pm 0.24$ | $0.49 \pm 0.31$ | $0.41 \pm 0.29$ |
| second interface | $0.84 \pm 0.63$ | $0.63 \pm 0.52$ | $0.79 \pm 0.53$ | $0.63 \pm 0.42$ |
| third interface | $0.67 \pm 0.39$ | $0.54 \pm 0.42$ | $0.64 \pm 0.49$ | $0.60 \pm 0.58$ |
| LASIK flap | $0.97 \pm 0.45$ | $0.83 \pm 0.62$ | $NULL$ | $NULL$ |

Note: The first, second and third interfaces are respectively air-epithelium interface, epithelium-Bowman's interface, and endothelium-aqueous interface; First Expert (second trained) manual grade to self represents intra-observer repeatability of the first expert (second trained) manual grader; SD for standard deviation.

**TABLE 3. Comparison among the proposed method with method $V_A$ (without Kalman filtering) and method $V_B$ (without Kalman filtering and without HTC).**

| Average time for an image $(ms)$ | | | Mean error ± SD $(pixels)$ | | |
|---|---|---|---|---|---|
| Proposed | Method $V_A$ | Method $V_B$ | Proposed | Method $V_A$ | Method $V_B$ |
| 521 | 403 | 192 | $0.92 \pm 1.07$ | $1.43 \pm 2.57$ | $2.89 \pm 2.73$ |

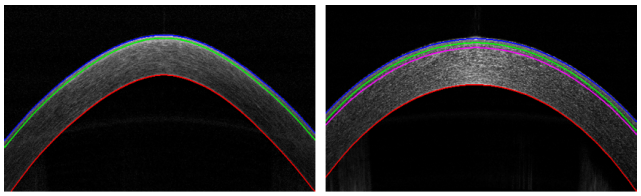

(a) (b)

**FIGURE 13. Robustness test for the proposed method with pathological images with (a) keratoconus and (b) LASIK flap. Note that the color blue, green, red and magenta curves represent the air-epithelium, epithelium-Bowman's, endothelium-aqueous and LASIK flap layer interfaces respectively.**

### C. ADDITIONAL EXPERIMENTS

To elaborate the roles of Kalman filtering and HTC, two variants were devised and tested. One variant was to use the proposed algorithm without Kalman filtering, i.e., taking the fitted circle as the layer interface, which was denoted as method $V_A$; and the other variant was to take the output of customized edge detection as the layer interface, without the use of HTC and Kalman fitting, which was denoted as method $V_B$. Figure 11(c) shows the segmented endothelium-aqueous interfaces by the proposed method, method $V_A$ and method $V_B$.

## IV. DISCUSSION AND CONCLUSION

### A. ROLES OF KALMAN FILTERING AND HOUGH TRANSFORM

The customized HTC can significantly enhance the layer interface accuracy (from 2.89±2.73 to 1.43±2.57 pixels, comparison between methods $V_B$ and $V_A$, Table 3), which may reflect the fact that the corneal layer interface can be well represented by a carefully designed circle to handle well interface boundaries that are difficult to determine (such as broken or unclear interface boundaries as shown by Fig. 11(c). Note that the interface boundaries of methods $V_A$ and $V_B$ are in cyan and green respectively.).

Kalman filtering can further enhance the accuracy of the fitted circle significantly (from 1.43±2.57 to 0.92±1.07 pixels, comparison between method $V_A$ and the proposed method, Table 3), which may imply that Kalman filtering can effectively handle the heavy noise exhibited in the image and could be adapted to shape variation from a circle to be closer to the real layer interface through a correction mechanism (Fig. 11(c), the interface of method $V_A$ and the interface of the proposed method are displayed by the color cyan and magenta respectively).

### B. COMPARISON WITH EXISTING METHODS

The performance of existing methods is to be compared in terms of computational cost and accuracy.

Semi-automated segmentation of five corneal layer interfaces for a single image (with 512 × 512 pixels) can take as long as 20 seconds [26]. The average computation time is 1130 milliseconds per B-scan for 3 layer interfaces using parallel processing with 8 threads [30]. It takes 102±8 s to segment the corneal anterior and posterior interfaces with 816 × 636 pixels [31]. As to processing SD-OCT volumetric data, the segmentation of anterior and posterior surface took 141±8 s on average for a volume with 16 images (1024 × 256 pixels) [32]. The proposed method segments 3 layer interfaces within 521 ms for an image, which is substantially faster than the existing methods.

Jahromi *et al.* [26] reported a semi-automated method to achieve an overall mean absolute interface differences within 1.5 pixels. Similar accuracies were achieved with fully-automated methods to be in the range of 1-3 pixels: 1.5±0.4 pixels for air-epithelium interface, 1.2±0.5 pixels for epithelium-Bowman's interface, and 2.1±2.3 pixels for endothelium-aqueous interface [30]; 1.56±0.53 pixels for anterior interface and 2.90±1.32 pixels for posterior interface [31]; 1.10±0.33 pixels for anterior surface and 1.75±0.60 pixels for posterior surface [32]. As these

accuracies are from segmentation of different data, it is inherently hard to judge which approach yields the best accuracy, since the segmentation accuracy depends on other factors in addition to approaches, such as imaging methodology (TD-OCT or SD-OCT), the imaging quality, and lateral and axial resolutions.

We have attempted to directly compare with existing methods using common datasets. The presented approach has been compared with LaRocca's approach on a common dataset [30]. From Table 1, it could be seen that the presented approach yields better or similar accuracy as compared with the results of [30], and all the mean absolute differences of the presented approach were smaller than that of the two references from the two manual graders. Paired t-tests were carried out to find that the proposed method yields significantly better accuracy for air-epithelium interface ($p < 0.016$) and epithelium-Bowman's interface ($p < 0.013$) than [30]. As for endothelium-aqueous interface, the proposed method yields smaller mean absolute differences ($1.59 \pm 2.04$ pixels versus $1.66 \pm 2.15$ pixels) than [30], but the difference is not significant ($p < 0.052$).The proposed method is 2.17 (1130/521) times faster than the existing technique with inferior software environment to derive the 3 layer interfaces of an image.

### C. ADVANTAGES

The recent evolution of OCT from time-domain to spectral-domain has increased substantially acquisition speed and made imaging of volumetric data with huge number of bytes feasible. Therefore, fast and automatic segmentation of layers and thickness measurement for SD-OCT data has increasingly become more important than ever. Our purpose is to minimize processing time while maintaining accurate and reliable segmentation. The proposed method has the following advantages.

#### 1) FAST

The mean time load of the presented approach to detect 3 layer interfaces is 521 *ms* for an image, while existing approaches will take more than one second [27]–[32]. The low computational load can be attributed mainly to the framework of the presented approach: image projection to initialize the corneal apex, a customized HTC with low complexity, approximating the 3 layer interfaces with 1D difference of intensity mean along axial direction, Savitzsky-Golay smoothing with pre-calculated weights, and Kalman filtering with low order ($2 \times 2$) matrix manipulation to track boundaries.

#### 2) ACCURATE

The presented approach yields significantly better or similar accuracy as compared with the existing method [30] (Table 1). This can be ascribed to the core components of the presented approach: employment of prior knowledge to derive ROIs, HTC to fit the layer interfaces to carefully designed circles, and Kalman filtering to perform well even in the presence of heavy noise and artifacts. Additional experiments (Table 2) showed that: 1) the customized HTC can significantly enhance the interface accuracy (from $2.89 \pm 2.73$ to $1.43 \pm 2.57$ pixels, comparison between methods $V_B$ and $V_A$), which may reflect the fact that the interface can be well represented by a carefully designed circle to handle well interface boundaries that are difficult to determine (such as broken or unclear interface boundaries as shown by Fig. 11(c)), and 2) Kalman filtering can further enhance the accuracy of the fitted circles significantly (from $1.43 \pm 2.57$ to $0.92 \pm 1.07$ pixels, comparison between methods $V_A$ and the proposed method). This implies that Kalman filtering handles well the heavy noise exhibited in the image and can be adapted to shape variation from a circle to be closer to the real layer interface through a correction mechanism (Fig. 11(c)).

### D. CONTRIBUTIONS AND LIMITATIONS

The novelties of the study are four-folds: determination of the parabolic curve's coefficient from its inscribed circle, customized HTC with low computational cost for modeling the interface shape, Kalman filtering to refine boundaries in each interface, and the customized edge detection to have a good initial approximation of each layer interface. All these contribute to substantial reduction of computational cost while preserving segmentation accuracy.

In particular, this study is focused on methodology and validation has been carried out for corneal layer interfaces in SD-OCT images of normal and pathological eye cases. The proposed method has introduced Kalman filtering based on the assumption the shape of layer interfaces can be a parabolic curve which renders itself to handle pathological cases. We have tested and quantified the method on pathological cases.

The presented approach is based on the following assumptions: the layer interfaces are visible in the images, central artifacts fall in the central region II, and different layer interfaces will not intersect. We humbly believe that the presented approach will be applicable to those pathologies as long as they will not invalidate these assumptions.

Experts are only able to obtain 3 layer interfaces due to image quality, and we opt to segment these layer interfaces to demonstrate the effectiveness of the methodology. We believe that the presented methodology can be easily extended for extraction of more layer interfaces when the imaging quality is enhanced to have clear boundaries of more layers.

To conclude, an approach to automatic segmentation of corneal layer interfaces from SD-OCT images has been presented and validated. A quantitative evaluation has been performed based on 20 B-scans covering the usually observed variability, by comparing the results with those delineated manually by two eye experts. For segmenting 3 layer interfaces on each B-scan, quantitative results show that the average absolute layer interface error is below 5.4 $\mu$m, being smaller than the difference between two eye experts manual delineations with an average processing time of 521 *ms* for an image. Our methodology has been compared with

state-of-the-art method [30] against a common dataset of normal eyes to yield significantly better or similar accuracy (Table 1) and is 2.17 times faster even with inferior software environment to derive the 3 layer interfaces of a B-scan. The proposed customized HTC can effectively represent the corneal layer interface for normal subjects, while Kalman filtering can handle the heavy noise exhibited in the image and can be adapted to shape variation to be closer to the real layer interface through a correction mechanism (Table 2). The presented approach can be a potential tool to quantify the corneal layer interfaces from SD-OCT. For further implementations, the methodology can be extended to more layer interfaces. It can be applied to eye diseases using computer assisted diagnosis systems that are based on SD-OCT and TD-OCT.

## V. DISCLOSURES

No conflicts of interest, financial or otherwise, are declared by the authors.

## ACKNOWLEDGMENT

The authors would like to thank Dr. Francesco LaRocca for providing the dataset introduced in paper [30], Prof. Hongbo Chen for his invaluable comments on Hough transform, Dr. Kelvin Wong for his efforts in enhancing the language usage, and Dr. Mingyang Chen and Mr. Haoyu Wang for their help in using LaTex.

## REFERENCES

[1] D. Huang *et al.*, "Optical coherence tomography," *Science*, vol. 254, no. 5035, pp. 1178–1181, 1991.

[2] J. G. Fujimoto, W. Drexler, J. S. Schuman, and C. K. Hitzenberger, "Optical coherence tomography (OCT) in ophthalmology: Introduction," *Opt. Exp.*, vol. 17, no. 5, pp. 3978–3979, 2009.

[3] J. A. Izatt *et al.*, "Micrometer-scale resolution imaging of the anterior eye *in vivo* with optical coherence tomography," *Arch. Ophthalmol.*, vol. 112, no. 12, pp. 1584–1589, 1994.

[4] S. Radhakrishnan *et al.*, "Real-time optical coherence tomography of the anterior segment at 1310 nm," *Arch. Ophthalmol.*, vol. 119, no. 8, pp. 1179–1185, 2001.

[5] M. K. Garvin, M. D. Abramoff, X. Wu, S. R. Russell, T. L. Burns, and M. Sonka, "Automated 3-D intraretinal layer segmentation of macular spectral-domain optical coherence tomography images," *IEEE Trans. Med. Imag.*, vol. 28, no. 9, pp. 1436–1447, Sep. 2009.

[6] K. Lee, M. Niemeijer, M. K. Garvin, Y. H. Kwon, M. Sonka, and M. D. Abramoff, "Segmentation of the optic disc in 3-D OCT scans of the optic nerve head," *IEEE Trans. Med. Imag.*, vol. 29, no. 1, pp. 159–168, Jan. 2010.

[7] S. J. Chiu, X. T. Li, P. Nicholas, C. A. Toth, J. A. Izatt, and S. Farsiu, "Automatic segmentation of seven retinal layers in SDOCT images congruent with expert manual segmentation," *Opt. Exp.*, vol. 18, no. 18, pp. 19413–19428, 2010.

[8] I. Jones, T. J. Rainsford, B. Fischer, and D. Abbott, "Towards T-ray spectroscopy of retinal isomers: A review of methods and modelling," *Vibrat. Spectrosc.*, vol. 41, no. 2, pp. 144–154, Aug. 2006.

[9] X. Yin, B. W.-H. Ng, J. He, Y. Zhang, and D. Abbott, "Accurate image analysis of the retina using hessian matrix and binarisation of thresholded entropy with application of texture mapping," *PLoS One*, vol. 9, no. 4, p. e95943, 2014.

[10] L. Fang, S. Li, X. Kang, J. A. Izatt, and S. Farsiu, "3-D adaptive sparsity based image compression with applications to optical coherence tomography," *IEEE Trans. Med. Imag.*, vol. 34, no. 6, pp. 1306–1320, Jun. 2015.

[11] L. Fang, S. Li, D. Cunefare, and S. Farsiu, "Segmentation based sparse reconstruction of optical coherence tomography images," *IEEE Trans. Med. Imag.*, vol. 36, no. 2, pp. 407–421, Feb. 2017.

[12] Y. Li, R. Shekhar, and D. Huang, "Corneal pachymetry mapping with high-speed optical coherence tomography," *Ophthalmology*, vol. 113, no. 5, pp. 792.e2–799.e2, May 2006.

[13] Y. Li, M. V. Netto, R. Shekhar, R. R. Krueger, and D. Huang, "A longitudinal study of LASIK flap and stromal thickness with high-speed optical coherence tomography," *Ophthalmology*, vol. 114, no. 6, pp. 1124.e1–1132.e1, 2007.

[14] N. Hutchings *et al.*, "Swelling of the human cornea revealed by high-speed, ultrahigh-resolution optical coherence tomography," *Invest. Ophthalmol. Vis. Sci.*, vol. 51, no. 9, pp. 4579–4584, 2010.

[15] G. O. Waring, III, W. M. Bourne, H. F. Edelhauser, and K. R. Kenyon, "The corneal endothelium: Normal and pathologic structure and function," *Ophthalmology*, vol. 89, no. 6, pp. 531–590, Jun. 1982.

[16] B. A. Holden, G. W. Mertz, and J. J. McNally, "Corneal swelling response to contact lenses worn under extended wear conditions," *Invest. Ophthalmol. Vis. Sci.*, vol. 24, pp. 218–226, Feb. 1983.

[17] M. R. O'Neal and K. A. Poise, "*In vivo* assessment of mechanisms controlling corneal hydration," *Invest. Ophthalmol. Vis. Sci.*, vol. 26, no. 6, pp. 849–856, 1985.

[18] H. Cheng, A. K. Bates, L. Wood, and K. McPherson, "Positive correlation of corneal thickness and endothelial cell loss. Serial measurements after cataract surgery," *Arch. Ophthalmol.*, vol. 106, no. 7, pp. 920–922, 1988.

[19] R.-P. Copt, R. Thomas, and A. Mermoud, "Corneal thickness in ocular hypertension, primary open-angle glaucoma, and normal tension glaucoma," *Arch. Ophthalmol.*, vol. 117, no. 1, pp. 14–16, 1999.

[20] J. D. Brandt, J. A. Beiser, M. O. Gordon, and M. A. Kass,, "Central corneal thickness and measured IOP response to topical ocular hypotensive medication in the ocular hypertension treatment study," *Amer. J. Ophthalmol.*, vol. 138, no. 5, pp. 717–722, Nov. 2004.

[21] M. Zhao, A. N. Kuo, and J. A. Izatt, "3D refraction correction and extraction of clinical parameters from spectral domain optical coherence tomography of the cornea," *Opt. Exp.*, vol. 18, no. 9, pp. 8923–8936, 2010.

[22] Y. Li, R. Shekhar, and D. Huang, "Segmentation of 830- and 1310-nm LASIK corneal optical coherence tomography images," *Proc. SPIE*, vol. 4684, pp. 167–178, May 2002.

[23] C. Lal, J. McGrath, H. Subhash, S. Rani, T. Ritter, and M. Leahy, "Quantitative assessment of rat corneal thickness and morphology during stem cell therapy by high-speed optical coherence tomography," *Proc. SPIE*, vol. 9693, pp. 96931U-1–96931U-7, Mar. 2016.

[24] H. Rabbani *et al.*, "Obtaining thickness maps of corneal layers using the optimal algorithm for intracorneal layer segmentation," *Int. J. Biomed. Imag.*, vol. 2016, Apr. 2016, Art. no. 1420230.

[25] F. Wang *et al.*, "Automated boundary segmentation and wound analysis for longitudinal corneal OCT images," *Proc. SPIE*, vol. 10137, pp. 1013708-1–1013708-8, Mar. 2017.

[26] M. K. Jahromi *et al.*, "An automatic algorithm for segmentation of the boundaries of corneal layers in optical coherence tomography images using Gaussian mixture model," *J. Med. Signals Sens.*, vol. 4, no. 3, pp. 171–180, Jul. 2014.

[27] J. Eichel, A. Mishra, D. Clausi, P. Fieguth, and K. Bizheva, "A novel algorithm for extraction of the layers of the cornea," in *Proc. IEEE Can. Conf. Comput. Robot Vis.*, Kelowna, BC, Canada, May 2009, pp. 313–320.

[28] M. Shen, L. Cui, M. Li, D. Zhu, M. R. Wang, and J. Wang, "Extended scan depth optical coherence tomography for evaluating ocular surface shape," *J. Biomed. Opt.*, vol. 16, no. 5, p. 056007, 2011.

[29] P. Shu and Y. Sun, "Automated extraction of the inner contour of the anterior chamber using optical coherence tomography images," *J. Innov. Opt. Health Sci.*, vol. 5, no. 4, p. 1250030, 2012.

[30] F. LaRocca, S. J. Chiu, R. P. McNabb, A. N. Kuo, J. A. Izatt, and S. Farsiu, "Robust automatic segmentation of corneal layer boundaries in SDOCT images using graph theory and dynamic programming," *Biomed. Opt. Exp.*, vol. 2, no. 6, pp. 1524–1538, 2011.

[31] D. Williams, Y. Zheng, F. Bao, and A. Elsheikh, "Automatic segmentation of anterior segment optical coherence tomography images," *J. Biomed. Opt.*, vol. 18, no. 5, p. 056003, May 2013.

[32] D. Williams, Y. Zheng, P. G. Davey, F. Bao, M. Shen, and A. Elsheikh, "Reconstruction of 3D surface maps from anterior segment optical coherence tomography images using graph theory and genetic algorithms," *Biomed. Signal Process. Control*, vol. 25, pp. 91–98, Mar. 2016.

[33] T. Zhang *et al.*, "Fast retinal layer segmentation of spectral domain optical coherence tomography images," *J. Biomed. Opt.*, vol. 20, no. 9, p. 096014, Sep. 2015.

[34] R. E. Kalman, "A new approach to linear filtering and prediction problems," *J. Basic Eng.*, vol. 82, no. 1, pp. 35–45, Mar. 1960.

[35] P. Viola and M. Jones, "Rapid object detection using a boosted cascade of simple features," in *Proc. IEEE Conf. Comput. Vis. Pattern Recognit.*, vol. 1. Dec. 2001, pp. 511–518.
[36] D. Marr and E. Hildreth, "Theory of edge detection," *Proc. Roy. Soc. London B, Biol. Sci.*, vol. 207, pp. 187–217, Feb. 1980.
[37] A. Savitzky and M. J. E. Golay, "Smoothing and differentiation of data by simplified least squares procedures," *Anal. Chem.*, vol. 36, no. 8, pp. 1627–1639, 1964.
[38] S. Heegaard and H. Grossniklaus, Eds., *Eye Pathology: An Illustrated Guide*, 1st ed. Berlin, Germany: Springer-Verlag,2015.
[39] G. Smith and D. A. Atchison, *The Eye and Visual Optical Instruments*. Cambridge, U.K.: Cambridge Univ. Press, 1997.
[40] M. Z. M. Jafri and F. Deravi, "Efficient algorithm for the detection of parabolic curves," *Proc. SPIE*, vol. 2356, p. 53, Jan. 1995.
[41] P. Mukhopadhyay and B. B. Chaudhuri, "A survey of Hough transform," *Pattern Recognit.*, vol. 48, no. 3, pp. 993–1010, Mar. 2015.
[42] G. L. Foresti, C. S. Regazzoni, and G. Vernazza, "Circular arc extraction by direct clustering in a 3D Hough parameter space," *Signal Process.*, vol. 41, no. 2, pp. 203–224, Jan. 1995.
[43] G. E. Martin, *The Foundations of Geometry and the Non-Euclidean Plane*, 1st ed. New York, NY, USA: Springer-Verlag, 1975.
[44] R. Bronson, *Matrix Methods: An Introduction*, 2nd ed. San Diego, CA, USA: Academic, 1991.
[45] C. K. Chui and G. Chen, *Kalman Filtering With Real-Time Applications*, 4th ed. Berlin, Germany: Springer-Verlag, 2009.
[46] P. A. Gorry, "General least-squares smoothing and differentiation by the convolution (Savitzky–Golay) method," *Anal. Chem.*, vol. 62, no. 6, pp. 570–573, 1990.
[47] R. A. Serway and C. Vuille, *College Physics*. Boston, MA, USA: Cengage Learning, 2014.

**TIANQIAO ZHANG** was born in Hunan, China, in 1975. He received the M.S. degree in circuits and systems from Guangxi Normal University in 2006. He is currently pursuing the Ph.D. degree with the Research Lab for Medical Imaging and Digital Surgery, Shenzhen Institutes of Advanced Technology, University of Chinese Academy of Sciences. From 2006 to 2009, he has been a Software Engineer with Huawei Technologies Co., Ltd. Subsequently, he became a Senior Engineer and a Team Leader with the OCT Image Analysis Group, Shenzhen Moptim Imaging Technique Co., Ltd. His research interests include medical image processing and computer vision.

**AHMED ELAZAB** was born in Mansoura, Egypt, in 1984. He received the M.S. degree in computer science from Mansoura University, Egypt, in 2010, and the Ph.D. degree in pattern recognition and intelligent system from the Shenzhen Institutes of Advanced Technology, University of Chinese Academy of Sciences, China, in 2017. He is currently a Lecturer with the Computer Science Department, Misr Higher Institute for Commerce and Computers, Mansoura. His main research interests include medical image analysis and computer-aided diagnosis. He received the best paper award of the 7th Cairo International Biomedical Engineering Conference (IEEE/EMB). He has two outstanding student awards from the Shenzhen Institutes of Advanced Technology.

Dr. Elazab has authored and coauthored more than 15 peer-reviewed papers and has served as a reviewer in prestigious peer-reviewed international journals.

**XIAOGANG WANG** was born in China in 1981. He received the M.D. degree from Shanghai Jiao Tong University in 2014. He is currently a Resident of Ophthalmology with the Shanxi Eye Hospital. He is also an International Fellow with the Casey Eye Institute in 2012, and a Consultant at various medical institutions. He has published two significant papers in ophthalmology, and has written two books on the topic of glaucoma, and OCT angiography of the eye. He also has a patent in his field of research, and has been supported by the National Science Foundation of China and several Shenzhen research grants. His research activities are mainly on ophthalmic imaging technologies for the eye, and in the field of optical coherence tomography, and Scheimflug imaging technology.

**FUCANG JIA** was born in Hebei, China, in 1976. He received the B.S. degree in applied mathematics from the Beijing Institute of Technology in 1998, the M.S. degree in biological psychology from the Institute of Psychology, Chinese Academy of Sciences, in 2001, and the Ph.D. degree in computer application technology from the Institute of Computing Technology, Chinese Academy of Sciences, in 2004. In 2004, he joined the Department of Surgical Instruments, Shenzhen Anke Co., Ltd., as a Research and Development Engineer, then as a Project Manager and a Department Manager. Since 2008, he has been with the Center for Human–Computer Interaction, Shenzhen Institutes of Advanced Technology, Chinese Academy of Sciences, as a Principal Investigator, and since 2012, he has been with the Research Lab for Medical Imaging and Digital Surgery. He has been funded with ten grants by the National Key Research and Development Program, the key Union Foundation of the National Science Foundation of China and Guangdong Province, and the key Guangdong Provincial Science and Development Program. He has authored or co-authored for over 100 articles and holds eight patents of invention. His current research interests include computer-assisted medical interventions, brain imaging, and machine learning.

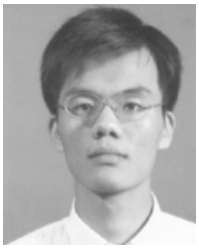

**JIANHUANG WU** received the Ph.D. degree from the Shenyang Institute of Automation, Chinese Academy of Sciences, in 2007. He is currently an Associate Professor and a Principal Investigator with the Research Laboratory for Medical Imaging and Digital Surgery, Shenzhen Institutes of Advanced Technology, Chinese Academy of Sciences. He has been funded with grants by the National Key Research and Development Program, the key Union Foundation of the National Science Foundation of China and Guangdong Province, and the key Guangdong Provincial Science and Development Program. He has authored over 60 journal articles, and has achieved over ten patent awards. His research interests include virtual surgery, medical visualization, and computer graphics. He has also been nominated by the Chinese Academy of Sciences into the board of outstanding creative scientists, and has been received with the title of Shenzhen's Distinguished High Profile Professional.

**GUANGLIN LI** (SM'06) received the Ph.D. degree in biomedical engineering from Zhejiang University, China, in 1997. From 1999 to 2002, he was a Post-Doctoral Research Associate with the Department of Bioengineering, University of Illinois at Chicago, where he was involved in electrocardiography and electroencephalography inverse problems and cardiac electrophysiology. From 2002 to 2006, he was a Senior Research Scientist with BioTechPlex Corporation, where he was involved in the research and development of biomedical and biological products. From 2006 to 2009, he was with the Rehabilitation Institute of Chicago (the best rehabilitation hospital in America for 19 consecutive years), where he was a Senior Research Scientist with the Neural Engineering Center for Artificial Limbs. Then, he has been with Northwestern University, where he was an Assistant Professor of Physical Medicine and Rehabilitation, Chicago. Since 2009, he has been with the Shenzhen Institute of Advanced Technology, Chinese Academy of Sciences, and is currently a Professor with the Research Center for Neural Engineering, Institute of Biomedical and Health Engineering.

Dr. Li has authored over 50 peer-reviewed papers in biomedical engineering and rehabilitation engineering. He has served as a Reviewer for over ten peer-reviewed international journals, an international Board Advisory of the journal, *Physiological Measurement*, and is the an Associate Editor of the IEEE TRANSACTIONS ON INFORMATION AND TECHNOLOGY IN BIOMEDICINE.

**QINGMAO HU** was born in Hubei, China, in 1963. He received the B.S. degree in electromagnetic measurement and instrumentation from Hunan University in 1984, the M.S. degree in automation theory and its applications from the Harbin Institute of Technology in 1986, and the Ph.D. degree in industrial automation from the Huazhong University of Science and Technology in 1990, respectively. He has served as a Lecturer, an Associate Professor, and a Professor with the First Military Medical University from 1990 to 1996, and was a Guest Scientist and a Post-Doctoral Fellow with the University of Bern, Switzerland, from 1996 to 2000. From 2000 to 2007, he served as an Associate Member, a member, and a Senior Scientist with the Biomedical Imaging Lab, Agency of Science, Technology and Research of Singapore. He joined the Shenzhen Institute of Advanced Technology, Chinese Academy of Sciences, as a Professor and the Director of the Research Lab for Medical Imaging and Digital Surgery. He has proposed the medical image segmentation framework based on prior knowledge, and has developed several robust image analysis systems utilized clinically, especially on the computer-aided system for stroke. His works have been utilized in national clinical and international cooperation institutions. He has authored over 110 papers, filed over 20 international patents. His major research areas are image analysis, robust medical image processing, computer-aided diagnoses and therapy, computer vision, and pattern recognition. He was honored with the Hundred Talent of CAS in 2008 and a Distinguished Professor of Shenzhen in pattern recognition and intelligence system in 2010. He received the RSNA third prizes for three times, the ASNR first prize for one time, the Scientific and Technological Progress Award of the PLA twice, and the National Invention Award fourth prize for one time.